

PACS numbers: 42.30.Wb, 87.57.nf, 87.63.lt
DOI: 10.1070/QE2014v044n07ABEH015419

Differential visualisation of a spectrally selective structure of strongly scattering objects

A.S. Kuratov, K.V. Rudenko, V.V. Shuvalov

Abstract. **We describe a modification of the algorithm for the fast approximate solution of the diffuse optical tomography inverse problem. In this modification the amount of *a priori* (auxiliary) information necessary for the visualisation of the internal structure of the object is reduced by using a differential measurement scheme. The experiment is performed at two different wavelengths, and some *a priori* information, necessary to reconstruct only the spectrally selective component of the internal structure (the difference structure of the spatial distributions of the extinction coefficient at the wavelength employed), is replaced by the data of one of these measurements.**

Keywords: *diffuse optical tomography, multiple small-angle scattering, approximate solution of the inverse problem, differential measurements, reconstruction of the spectrally selective internal structure.*

1. Introduction

Diffuse optical tomography (DOT) is one of the most promising methods of noninvasive medical diagnostics [1]. The capabilities of DOT have been approved in mammography [2–7] and in the problems of functional brain imaging [8–11]. Recently, DOT has been suggested to be employed for monitoring during phototherapy [12]. Many papers have been already published on fluorescence DOT [12–14], direct and inverse problems of which are similar (by the methods of the solutions) to the so-called transmission DOT (see below).

In DOT, a strongly scattering object (hereinafter, an object), the internal structure of which must be visualised, is exposed many times [for different positions of the emitter and receiver $i = (x_i, y_i)$ and $j = (x_j, y_j)$, respectively, on the surface of the object $\{x, y\}$; hereinafter, $\{i,j\}$-measurements] to near-IR radiation. For all realisations (sets of points $\{i,j\}$), the parameters (in the case of cw irradiation it is usually the power) of the output radiation are measured. As a result, we obtain a matrix Φ_{ij} of the output data, which characterises the properties of the object. The number of the elements of this matrix, $N = N_i N_j$, is given by the number of the involved positions of the emitter and the receiver, $i,j = 0, 1, \ldots, (N_{i,j} - 1)$.

A.S. Kuratov, K.V. Rudenko, V.V. Shuvalov Department of Physics, M.V. Lomonosov Moscow State University, Vorob'evy gory, 119991 Moscow, Russia; International Laser Center, M.V. Lomonosov Moscow State University, Vorob'evy gory, 119991 Moscow, Russia; e-mail: vsh@vsh.phys.msu.su

Received 24 February 2014; revision received 4 May 2014
Kvantovaya Elektronika **44** (7) 652–656 (2014)
Translated by I.A. Ulitkin

Then, using these data, the so-called inverse problem is solved (the internal structure of the object is visualised), i.e., ideally, the desired 3D spatial distribution of the absorption $\mu_a(\boldsymbol{r})$ and scattering $\mu_s'(\boldsymbol{r})$ coefficients, the anisotropy parameter of the single photon scattering indicatrix $\gamma(\boldsymbol{r})$, etc. are calculated.

The authors of [15–19] described the algorithm, which, for a fast solution of the inverse DOT problem, utilises additional *a priori* information along with the data matrix Φ_{ij}. These are, firstly, a reference matrix $\Phi_{ij}^{(1)}$ describing the results of the same measurements for a strongly scattering object but without an internal structure (hereinafter referred to as a reference object) and, secondly, 3D distributions $f_{ij}^{(1)}(\boldsymbol{r})$ of the probability density of passage of the photons, detected in each $\{i,j\}$-measurement, through an arbitrary point $\boldsymbol{r}$ of the reference object. The role of the visualised internal structure is played by the calculated 3D probability distribution $p_\Sigma^{(1)}(\boldsymbol{r})$, which allows one to find inside the object the inhomogeneities that additionally (with respect to the reference object) attenuate the detected radiation fluxes in a real object (Fig. 1). In implementing this algorithm in [15–17], all *a priori* data were calculated on the basis of the information about the size, shape and nature of the object with the use of fast approximate methods for solving the direct DOT problem. Tret'yakov et al. [18] have shown that the accuracy with which $p_\Sigma^{(1)}(\boldsymbol{r})$ represents the real internal structure is not always satisfactory, and have suggested an iterative version of the same algorithm. In this case, the data $p_\Sigma^{(n)}(\boldsymbol{r})$, obtained by the nth iteration of the algorithm, are used to calculate *a priori* information for the $(n + 1)$th iteration. It has been shown that with increasing n, the accuracy of the internal object structure reconstruction

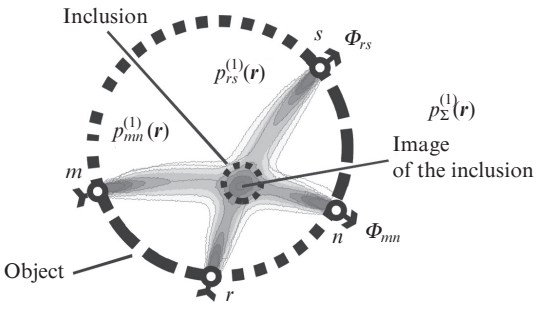

Figure 1. Fast algorithm for the approximate solution of the inverse DOT problem: Φ_{mn} and Φ_{rs} are the photon fluxes for $\{m,n\}$- and $\{r,s\}$-measurements. The object structure is described by the function $p_\Sigma^{(1)}(\boldsymbol{r}) = p_{mn}^{(1)}(\boldsymbol{r}) + p_{rs}^{(1)}(\boldsymbol{r})$ of the probability distribution for finding inclusions inside the object that additionally (relative to the reference object) attenuate the detected radiation fluxes.

increases, and this structure exhibits even relatively small details [18, 19].

The main disadvantage of the algorithm described is a large amount of *a priori* information necessary for its implementation. Moreover, the stronger the difference of the real object from the reference one (i.e., the more complex the structure of the real object and the less accurate the *a priori* information), the worse the convergence of the algorithm and the accuracy, which is realised in the first iteration. Naturally, more time will be required to achieve the specified accuracy of visualisation of the internal structure. Furthermore, the approbation of the algorithm by the authors [18] showed the possibility of emergence of systematic errors (irremovable within the method employed) related to the inaccuracy of *a priori* information.

In this paper we describe a modification of the algorithm discussed above, in which the amount of *a priori* information needed for fast visualisation of a spectrally selective internal structure of the object, is reduced as a result of the transition to a differential measurement scheme. In this case, the experiment is performed at two different wavelengths, $\lambda_{1,2}$; a part of the *a priori* information [the reference matrix $\Phi_{ij}^{(1)}$] is replaced with the data of one measurement – $\Phi_{ij}(\lambda_1)$, while the data of the second measurement, $\Phi_{ij}(\lambda_2)$, are used to reconstruct only the spectrally selective component of the internal structure of the object (i.e., the difference structure of spatial 3D distributions of the extinction coefficient at wavelengths $\lambda_{1,2}$).

2. Differential modification of the reconstruction algorithm

It is easy to see that even the original version of the algorithm [15–19] is in fact differential, since it helps to reconstruct the differences of the internal structure of a real scattering object from the structure of an 'ideal' counterpart with a spatially uniform distribution of all parameters [$\mu_a(\boldsymbol{r})$, $\mu_s'(\boldsymbol{r})$, $\gamma(\boldsymbol{r})$, etc.] describing its interaction with photons.

At the first stage of this algorithm realisation (Fig. 2a), we find the difference $\Delta\Phi_{ij} = \Phi_{ij}^{(1)} - \Phi_{ij}$ between the data Φ_{ij} of a real experiment and the data $\Phi_{ij}^{(1)}$ of a thought experiment with an ideal object. Then, assuming that the difference between the results of these experiments is due to the difference of the internal structures of two objects, we use the formula $p_{ij}^{(1)} = (\Delta\Phi_{ij}/\Phi_{ij}^{(1)})f_{ij}^{(1)}(\boldsymbol{r})$ to calculate the 3D distribution of the probability density for finding the inclusions, which additionally attenuate the radiation flux in each of the $\{i,j\}$-measurements in the experiment with a real object. At the final stage, the results of all $\{i,j\}$-measurements are used to calculate the 3D distribution of the probability density for finding the additional inclusions in the real object,

$$p_\Sigma^{(1)}(\boldsymbol{r}) = \sum_{ij} p_{ij}^{(1)}(\boldsymbol{r}),$$

which corresponds to the data of all the measurements and plays the role of the reconstructed internal structure of the real object. If necessary, the described algorithm involves additional iterations which minimise the errors of the procedure used because the internal structure of the real object, found on the previous iteration,

$$p_\Sigma^{(n)}(\boldsymbol{r}) = \sum_{k=1}^{n} p_\Sigma^{(k)}(\boldsymbol{r}),$$

is used as the internal structure of the ideal object in a subsequent iteration. Naturally, when $n \sim 2$, fast calculation of *a priori* information becomes somewhat more complicated due to the spatial inhomogeneity of the structure of the reference object; as a result, all the needed calculations are performed with the use of some additional simplifying assumptions [18, 19].

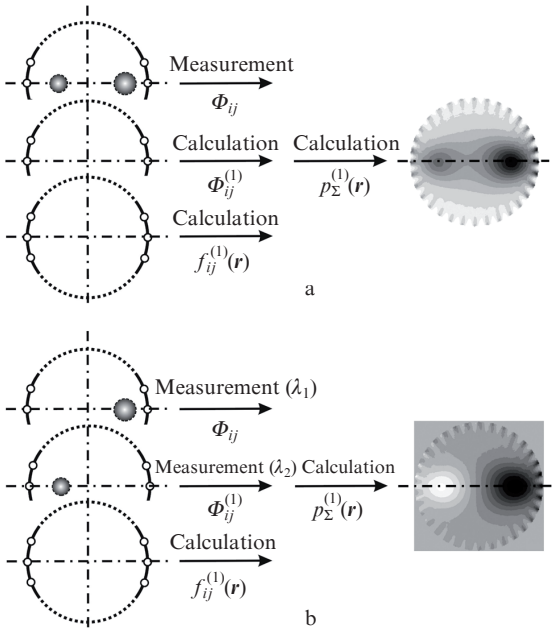

Figure 2. Input and output data for (a) the initial and (b) differential modifications of the algorithm for fast approximate solution of the inverse DOT problem.

The main disadvantage of the above-described algorithm is a very large amount of *a priori* information necessary for its implementation. While the errors of the latter decrease with increasing number of iterations used, the increase in the iteration number entails a reduction in the performance of the algorithm. However, one can not completely get rid of this information. Indeed, if the reference matrix $\Phi_{ij}^{(1)}$ may still be measured in a real experiment with an ideal object (which is still very difficult in practice), then finding a 3D distribution $f_{ij}^{(1)}(\boldsymbol{r})$ from the data of a real experiment is practically impossible.

With this in mind, we tested a new modification of the algorithm described above (Fig. 2b), in which the amount of *a priori* information needed for fast visualisation of the spectrally selective internal structure of the real object is reduced due to the use of a differential measurement scheme. In this modification, the experiment with the same real object is performed at two different wavelengths ($\lambda_{1,2}$). A part of the *a priori* information [the reference matrix $\Phi_{ij}^{(1)}$] is replaced by the data of one of these measurements, $\Phi_{ij}(\lambda_1)$, while the data of the second measurement, $\Phi_{ij}(\lambda_2)$, are used as the data matrix to reconstruct the spectrally selective component of the internal structure of the real object, i.e., the difference structure of the spatial distributions of the extinction coefficients at $\lambda_{1,2}$. It follows from the above said that the choice of the specific wavelengths λ_1 and λ_2 for measuring the reference matrix and the data one is in this case conditional, and the reconstructed differential structure may now contain the

regions with conditionally 'positive' $[\Phi_{ij}^{(1)}(\lambda_1) > \Phi_{ij}(\lambda_2)]$ and conditionally 'negative' $[\Phi_{ij}^{(1)}(\lambda_1) < \Phi_{ij}(\lambda_2)]$ extinction coefficients.

The main problem of such a modification of the algorithm is that the 3D distributions of $f_{ij}^{(1)}(\boldsymbol{r})$, required for the reconstruction of the internal structure of the object, can not be measured and replaced. However, given the fact that in real biological tissues the extinction coefficients are relatively small and the distributions of $f_{ij}^{(1)}(\boldsymbol{r})$ are very wide, we can try to keep them the same as those previously calculated for an ideal object.

Generally, the efficiency of the above-described quite incorrect procedures and the applicability of this modification of the algorithm are easier to be tested in a real model experiment considered in Sections 3 and 4.

3. Experimental setup

In the course of model experiments, we used a hardware-software complex, the block diagram of which is shown in Fig. 3a. The complex comprises two sources of cw radiation, (*1*). Radiation into/from a strongly scattering model object B with the internal structure (*3*) was launched/collected via a fibre switch (*2*) and two optomechanical switching systems, A and C. The latter select the numbers of the fibres (channels), through which, during each specific measurement, the input and output radiation is launched into and coupled out.

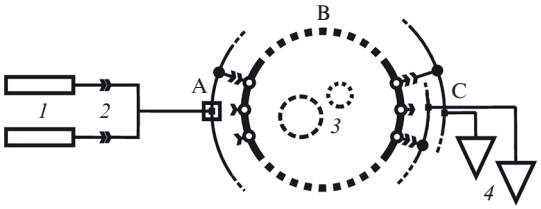

a

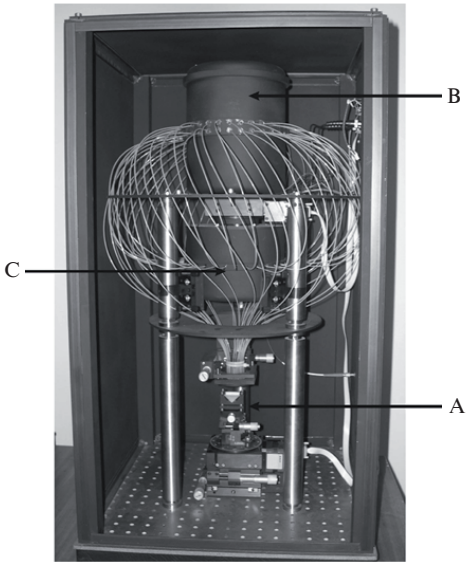

b

Figure 3. (a) Block diagram and (b) general view of the layout of the differential optical tomograph: (*1*) diode lasers; (*2*) optical fibres; (*3*) cylindrical inclusions; (*4*) photodetectors; (A) input optomechanical scanner; (B) strongly scattering cylindrical model object; (C) output optomechanical scanner.

Radiation transmitted through the model object is simultaneously detected in two channels by two identical photodetectors (*4*), which allows the time of full cycle measurements to be twice reduced. The software part of the complex is implemented by a personal computer (not shown in the block diagram) that provides the control of the hardware part of the complex, performs statistical processing of the measurement data and realisation of the algorithm described above.

Radiation sources are two cw diode lasers (JSC 'Semiconductor Devices', St. Petersburg) with a fibre output and a maximal power up to 500 mW at $\lambda_1 = 790$ nm and $\lambda_2 = 815$ nm that are completely appropriate for the differential determination of oxy- and deoxyhaemoglobin in blood. Radiation from the sources first enters the switch, wherein the images of both output fibre ends are transferred at a small angle to the input end of the main optical fibre (the core diameter of 800 μm, and the numerical aperture of 0.39). The attenuation coefficient in this case is ~4; however, the output power of both the sources is quite sufficient for the further measurements. Independent switching on/off of the power supplies of the two lasers allows for a situation where radiation propagates through the main optical fibre only at one of the two wavelengths (λ_1 or λ_2), at both wavelengths simultaneously or does not propagate at all.

Then, through the input switch the output radiation of the main fibre arrives at one of 32 input fibres. The main feature of this switch implementation is an extremely low (less than 10^{-4}) crosstalk noise level, which is very important because of the large dynamic range of the measurements performed.

The model object is a hollow cylindrical jar (inner diameter of 160 mm) filled with a mixture consisting of an aqueous emulsion with extremely small spherical fat droplets – Lipofundin (the emulsion is based on soybean oil emulsified with glycerol isotonic solution and contains oil droplets of size from 0.1 to 1.0 μm; it is an analogue of well-known fat emulsion, i.e., Intralipid, which is popular in the making of the biological tissue phantoms), playing the role of a small-angle scatterer, and an aqueous solution of black ink – an absorber. The component concentrations corresponded to $\mu_s' = 1.4$ mm^{-1} and $\mu_a = 0.005–0.015$ mm^{-1}. Along the perimeter of the jar in two horizontal planes shifted by 10 mm from the plane passing through the middle of the jar height, we symmetrically glued 32 input and 32 output optical fibres in staggered order. This order provided an additional (albeit very limited) ability to localise in vertical direction the positions of the visualised inclusions. Note also that the use of relatively thick (core diameter of 800 μm) output fibres with a large (0.39) numerical aperture ensured a more efficient collection of photons incident on the input ends of the optical fibres at sufficiently large angles from the scattering medium.

We placed in the model object several (up to three) long additional elements (inclusions) that simulate inhomogeneities of the internal structure. Blackened cylinders ('absolutely' absorbing inclusions) or various-diameter hollow glass cylinders with similar complex mixtures (with higher concentrations) played the role of the inclusions. Concentrations of the components in the cylinders were changed, allowing one to modify independently the optical characteristics of any of the inclusions. The geometry of their disposition also changed. The general view of the model object with the input and output switches and photodetectors is shown in Fig. 3b.

At any time moment, the two selected channels of the output switch were connected with two highly sensitive photodetectors (H6240-02 PMT units, Hamamatsu Inc.), operating in

the photon counting mode. The count pulses of the photodetectors in TTL format were counted with the help of a high-speed multi-channel counter (PCI 6602, National Instruments) within a time (up to 10 s) specified by the control computer. The count speed of dark pulses was only 100–150 pulse s^{-1}, which provides the ability to measure output light fluxes in a dynamic range of more than 10^4.

4. Results of testing the differential modification of the algorithm

As is clear from the previous section, the hardware of the complex was fully adapted to implement the differential measurement scheme, because the same model object could be used for measurements at two different wavelengths (790 and 815 nm). However, in all the test experiments carried out, we used only one light source ($\lambda_2 = 815$ nm), and for the differential visualisation of the internal structure of the object we used the results of two measurements performed for different geometries of the inclusions placed in the model object or for their different optical characteristics. In each of the measurements, a certain part from a total set of inclusions was removed to imitate its 'invisibility' at the corresponding wavelength (λ_1). As a result of two such measurements, we obtained two (necessary for the implementation of the differential modification of the algorithm) analogues of the data matrices $\Phi_{ij}(\lambda_1)$ and $\Phi_{ij}(\lambda_2)$, corresponding to 32 possible positions of the source and 32 possible positions of the detector. In the experiments on the reconstruction of the internal structures with semi-transparent inclusions, their displacement geometry in each of the two experiments remained the same, and two analogues of the data matrices $\Phi_{ij}(\lambda_1)$ and $\Phi_{ij}(\lambda_2)$, required for the implementation of the differential measurement scheme, corresponded to the measurements performed for various concentrations of the absorber (ink) in the same cylindrical inclusion.

Typical results of the reconstruction of the internal structure of a model object are illustrated in Fig. 4. Figure 4a shows the geometry of the model object with two opaque cylindrical inclusions of different size (radii $r_{1,2}$ = 15 and 10 mm) positioned at different ($R_{1,2}$ = 45 and 35 mm) distances from the symmetry axis of the object. Figures 4b and 4c present the grey-scale maps of $p_\Sigma^{(1)}(\boldsymbol{r})$ distributions obtained from the original and differential variants of the fast solution of the inverse DOT problem. The both maps use linear in $p_\Sigma^{(1)}$ shades of gray, but in the latter case, white colour (Fig. 4c) corresponds to the conditionally 'negative' values of the extinction coefficient (see Section 2), which is a direct consequence of a spatially inhomogeneous structure of the reference object. Absolute binding of $p_\Sigma^{(1)}$ to the specific values of optical characteristics of the inclusions is not a very difficult problem, but requires special calibration measurements, which must take into account a sufficiently large number of additional factors (finite angle of radiation collection by the output fibres, the possibility of multiple reflections of radiation by the walls of the inclusions, etc.).

Completely similar results were obtained in our experiments on the fast reconstruction of more complex internal structures with three inclusions, including semi-transparent ones, which indicates a relatively weak influence of the character of 3D distributions $f_{ij}^{(1)}(\boldsymbol{r})$ of the probability density of passage of the photons, detected in each $\{i,j\}$-measurement, through every point $\boldsymbol{r}$ of the reference object on the results of the reconstruction. Apparently, this is due to the fact that

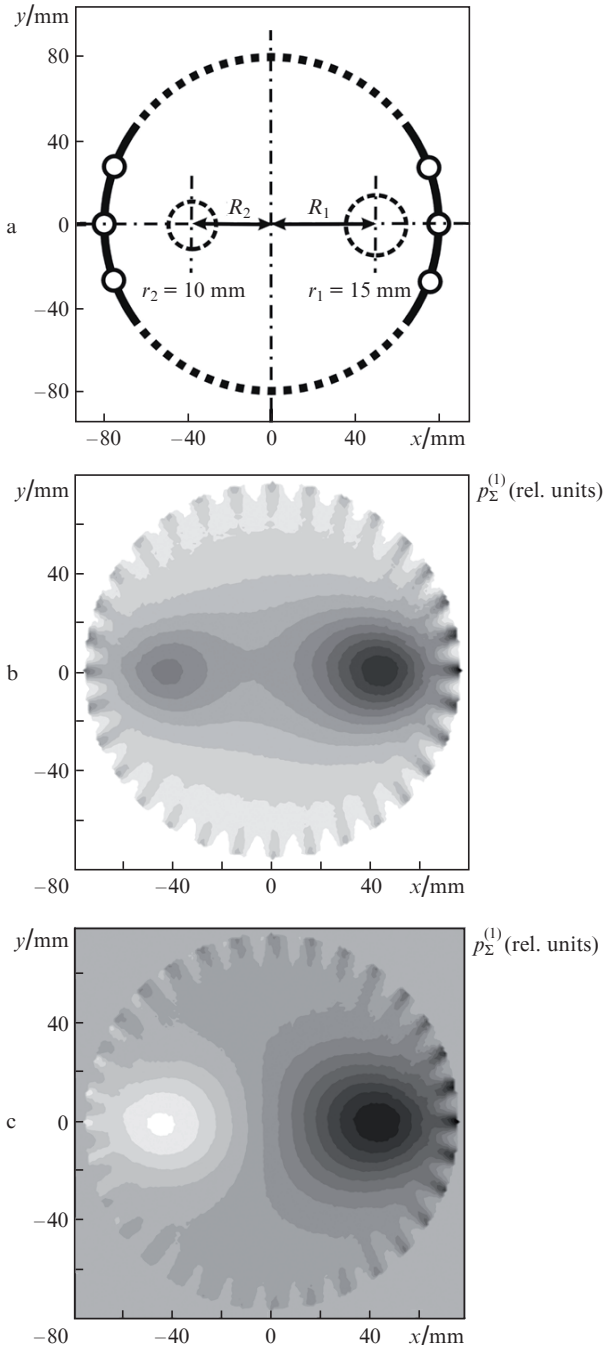

Figure 4. Geometry of the experiment (a) and maps (linear in $p_\Sigma^{(1)}$ shades of gray) of $p_\Sigma^{(1)}(\boldsymbol{r})$ distributions for the initial (b) and differential (c) variants of the inverse DOT problem solution. In the latter case, the white colour corresponds to 'negative' absorption.

when we use the optical characteristics of the model object ($\mu_s' = 1.4$ mm^{-1} and $\mu_a = 0.005–015$ mm^{-1}), which more or less correspond to the values for real biological tissues, the distributions $f_{ij}^{(1)}(\boldsymbol{r})$ are very broad, and in implementing the above-described replacement procedure, they can remain the same, i.e., corresponding to an ideal spatially uniform reference object.

5. Conclusions

Thus, this paper describes a modification of the projection algorithm for the fast approximate solution of the inverse

problem of diffuse optical tomography, in which the amount of *a priori* (auxiliary) information necessary for the visualisation of the internal structure of the object is reduced due to the use of a differential measurement scheme. In this case, the experiment with the same real object is performed at two different wavelengths, $\lambda_{1,2}$. A part of the *a priori* information [the reference matrix $\Phi_{ij}^{(1)}$] is substituted by the data of one of the measurements [$\Phi_{ij}(\lambda_1)$], while the data $\Phi_{ij}(\lambda_2)$ using the known [18, 19] procedure of the projection reconstruction can be employed to visualise the spectrally selective component of the internal structure of a real object (i.e., the difference structure of the spatial distributions of the extinction coefficient at wavelengths $\lambda_{1,2}$).

Results of testing the proposed modification of the algorithm in experiments with highly scattering and weakly absorbing ($\mu_s' = 1.4$ mm^{-1} and $\mu_a = 0.005-0.015$ mm^{-1}) model objects of sufficiently large (160 mm) size with a few (up to three) additional opaque and semi-transparent inclusions confirmed its operability and effectiveness.

References

1. Zimnyakov D.A., Tuchin V.V. *Kvantovaya Elektron.*, **32**, 849 (2002) [*Quantum Electron.*, **32**, 849 (2002)].
2. Ntziachristos V., Yodh A.G., Schnall M., Chance B. *Proc. Natl. Acad. Sci. USA*, **97**, 2767 (2000).
3. Pogue B., Poplack S.P., McBride T.O., Wells W.A., Osterman K.S., Osterberg U.L., Paulsen K.D. *Radiology*, **218**, 261 (2000).
4. Jiang H., Xu Y., Ifitimia N., Eggert J., Klove K., Baron L., Fajardo L. *IEEE Trans. Med. Imaging*, **20**, 1334 (2001).
5. Durduran T., Choe R., Culver J.P., Zubkov L., Holboke M.J., Giammarco J., Chance B., Yodh A. *Phys. Med. Biol.*, **47**, 2847 (2002).
6. Culver J.P., Choe R., Holboke M.J., Zubkov L., Durduran T., Slemp A., Ntziachristos V., Pattanayak D.N., Chance B., Yodh A. *Med. Phys.*, **30**, 235 (2003).
7. Gu X.J., Zhang Q.Z., Bartlett M., Schutz L., Fajardo L.L., Jiang H.B. *Acad. Radiol.*, **11**, 53 (2004).
8. Boas D.A., Brooks D.H., Miller E.L., Di Marzio C.A., Kilmer M., Gaudette R.J., Zhang Q. *IEEE Signal Process. Mag.*, **18**, 57 (2001).
9. Culver J.P., Durduran T., Furuya D., Cheung C., Greenberg J.H., Yodh A.G. *J. Cereb. Blood Flow Metab.*, **23**, 911 (2003).
10. Durduran T. *Ph.D. Thesis* (University of Pennsylvania, 2004).
11. Zeff B.W., White B.R., Dehghani H., Schlaggar B.L., Culver J.P. *Proc. Natl. Acad. Sci. USA*, **104**, 12169 (2007).
12. Wang H., Putt M.E., Emanuele M.J., Shin D.B., Glatstein E., Yodh A.G., Busch T.M. *Cancer Res.*, **64**, 7553 (2004).
13. Corlu1 A., Choe1 R., Durduran T., Rosen M.A., Schweiger M., Arridge S.R., Schnall M.D., Yodh A.G. *Opt. Express*, **15**, 6696 (2007).
14. Barletta W.R., Klanner F., Parmigiani F., Sauli D. *Appl. Opt.*, **571**, 203 (2007).
15. Chursin D.A., Shuvalov V.V., Shutov I.V. *Kvantovaya Elektron.*, **29**, 921 (1999) [*Quantum Electron.*, **29**, 83 (1999)].
16. Chursin D.A., Shuvalov V.V., Shutov I.V. *Laser Phys.*, **11**, 636 (2001).
17. Malikov E.V., Chursin D.A., Shuvalov V.V., Shutov I.V. *Kvantovaya Elektron.*, **30**, 78 (2000) [*Quantum Electron.*, **30**, 78 (2000)].
18. Tret'yakov E.V., Shuvalov V.V., Shutov I.V. *Kvantovaya Elektron.*, **31**, 1095 (2001) [*Quantum Electron.*, **31**, 1095 (2001)].
19. Tret'yakov E.V., Shuvalov V.V., Shutov I.V. *Kvantovaya Elektron.*, **32**, 941 (2002) [*Quantum Electron.*, **32**, 941 (2002)].